Biodegradation of herbicides by a plant nonheme iron dioxygenase: mechanism and selectivity of substrate analogues

DOI:
10.1002/chem.202103982

Document Version
Accepted author manuscript

Biodegradation of herbicides by a plant nonheme iron dioxygenase: mechanism and selectivity of substrate analogues

Yen-Ting Lin,[a] Hafiz S. Ali and Sam P. de Visser*[a]

[a] Mr Y.-T. Lin, Dr H. S. Ali, Dr S. P. de Visser
Manchester Institute of Biotechnology, The University of Manchester, 131 Princess Street, Manchester, M1 7DN, United Kingdom
[b] Mr Y.-T. Lin, Dr S. P. de Visser
Department of Chemical Engineering and Analytical Science, The University of Manchester, Oxford Road, Manchester, M13 9PL, United Kingdom
[c] Dr H. S. Ali
Department of Chemistry, The University of Manchester, Oxford Road, Manchester, M13 9PL, United Kingdom

Supporting information for this article is given via a link at the end of the document.

Abstract: Aryloxyalkanoate dioxygenases are unique herbicide biodegrading nonheme iron enzymes found in plants and hence, from environmental and agricultural point of view they are important and valuable. However, they often are substrate specific and little is known on the details of the mechanism and the substrate scope. To this end, we created enzyme models and calculate the mechanism for 2,4-dichlorophenoxyacetic acid biodegradation and 2-methyl substituted analogs by density functional theory. The work shows that the substrate binding is tight and positions the aliphatic group close to the metal center to enable a chemoselective reaction mechanism to form the C^2-hydroxy products, whereas the aromatic hydroxylation barriers are well higher in energy. Subsequently, we investigated the metabolism of *R*- and *S*-methyl substituted inhibitors and show that these do not react as efficiently as 2,4-dichlorophenoxyacetic acid substrate due to stereochemical clashes in the active site and particularly for the *R*-isomer give high rebound barriers.

Introduction

Herbicides are common chemicals used in agriculture to improve crop yield. Often, however, these chemicals cause toxicological and ecological problems to the environment.[1] As such, research has been devoted into biodegradable herbicides or environmentally friendly alternatives. Thus, herbicide biodegradation is important in agriculture and particularly from a human health perspective, whereby plants metabolize excess herbicide and prevent these chemicals from entering the human body or the environment. As a consequence a lot of scientific research has been devoted to studies into the efficiency and efficacy of these herbicides and their toxicological and environmental effects.[2]

In recent years a number of herbicides have been identified that are biodegradable by plants. In particular, herbicide resistant maize [3] and corn [4] crops were engineered with the aryloxyalkanoate dioxygenase (AAD) enzyme and found to be able to degrade the commonly used herbicide 2,4-dichlorophenoxyacetic acid (**2,4-D**) efficiently. This did not affect plant growth and led to herbicide biodegradation instead of its release into the environment.[4] Compounds like **2,4-D** (Scheme 1) are extensively used in agriculture as they are low-cost and effective.[5] Therefore, research has been performed into the activation of **2,4-D** and structural and functional analogues, such as *R*- and *S*-2-(2,4-dichlorophenoxy)propanoate (designated **RP** and **SP**). In particular, further use of aryloxyalkanoate dioxygenases in plant biotechnology and agriculture is being pursued. However, as little is known on the catalytic mechanism and substrate scope of these fascinating enzymes, we decided to do a computational study into the enzymatic reaction mechanism of AAD to shed light on its selectivity patterns.

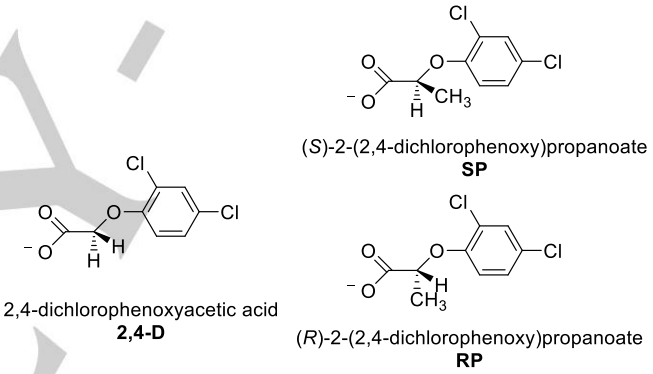

Scheme 1. Common dichlorophenoxy acids used in agriculture as herbicides.

Early studies on the enzyme AAD characterized it as a mononuclear nonheme iron hydroxylase that utilizes α-ketoglutarate (αKG; also called 2-oxoglutarate) and dioxygen.[6] Using ^{14}C isotopically labelled αKG it was established that the reaction produces $^{14}CO_2$ as products probably in a reaction with dioxygen. Moreover, gas chromatography-mass spectrometry measurements characterized succinate as a product. Based on these measurements, a catalytic cycle was proposed, whereby αKG binds to an iron(II) center and with dioxygen reacts to form an iron(IV)-oxo species and succinate upon release of CO_2. These nonheme iron(II) dioxygenases are widespread in nature and are involved in biosynthesis as well as biodegradation reactions.[7] For instance, the biosynthesis of antibiotics, such as viomycin and vancomycin, involves a nonheme iron dioxygenase,[8,9] while the metabolism of cysteine in the human body is triggered by the nonheme iron dioxygenase cysteine dioxygense.[10] For analogous nonheme iron dioxygenases, including taurine/αKG dioxygenase and prolyl-4-hydroxylase the iron(IV)-oxo species was trapped and characterized and it was shown to be the active oxidant in a reaction with deuterated substrate.[11,12]

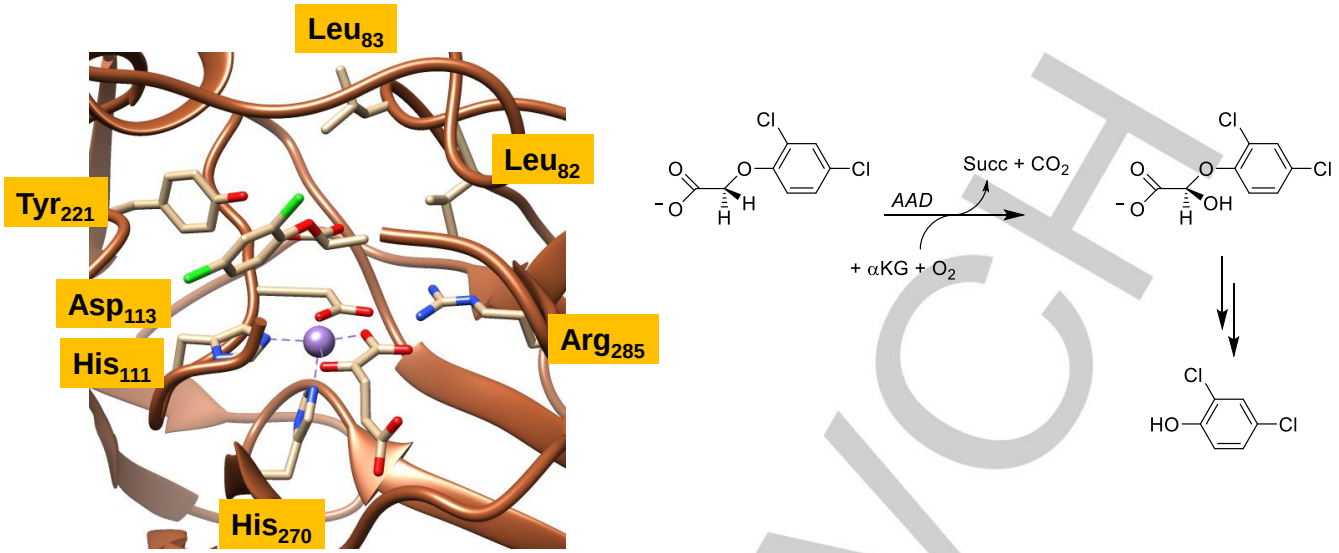

Figure 1. *Left*: Active site environment of *R*-2-(2,4-dichlorophenoxy)propanoate-bound AAD as taken from the 5BKB pdb file with key amino acid residues and Mn(II) ion highlighted. *Right*: Reaction mechanism of 2,4-dichlorophenoxyacetic acid biodegradation by AAD enzymes with Succ = succinate and αKG = α-ketoglutarate.

AAD is expected to convert **2,4-D** to its monohydroxylated product initially while in a subsequent step it is transformed into dichlorophenol, which was characterized as the final product. The latter is biodegraded by catechol dioxygenases to β-ketoadipate further. Details of the reaction mechanism are still elusive and the monohydroxylated product has never been characterized specifically. In addition to AAD, there are also enzymes, namely (*R*)- and (*S*)-dichlorprop/α-ketoglutarate dioxygenases (RdpA and SdpA), that activate the analogous substrates **RP** and **SP** (Scheme 1). The RdpA and SdpA enzymes show distinct differences in substrate binding pocket and hence do not fit the other enantiomer well and react highly enantiospecifically.[13] Even AAD, is known to activate **SP** but not **RP** efficiently although the reasons for this remain unknown.[14] The AAD amino acid sequence was determined [15] and a structure of AAD enzymes was crystallographically resolved. In Figure 1, we highlight the active site of AAD as based on the 5BKB protein databank (pdb) file.[16,17] Although the engineered structure has a central manganese(II) ion, the wildtype protein is a nonheme iron dioxygenase where the iron(II) is bound to the protein through a typical 2-His/1-Asp linkage with residues His_{111}, Asp_{113} and His_{270}. The crystal structure has the inhibitor *R*-2-(2,4-dichlorophenoxy)propanoate bound, which is located just above the plane of the metal-αKG group and its carboxylate group forms a hydrogen bonding interaction with the phenol group of Tyr_{221}, while several aliphatic amino acids (Leu_{82}, Leu_{83}) line the top of the substrate binding pocket. An active site Arg residue (Arg_{285}) does not appear to interact with the carboxylate of the substrate but is close to the metal-bound carboxylates of αKG and Asp_{113}.

Despite the fact that several biochemical studies investigated the substrate-scope, dioxygen usage and product distributions,[6,15,18] little is known on the details of the reaction mechanism of AAD and whether alternative substrates can be activated. Therefore, we pursued a computational study into the activation of **2,4-D**, **RP** and **SP** by AAD enzymes. As shown here, the substrate-binding pocket is tight and compact and enables little flexibility, which affects the reaction patterns for substrate hydroxylation. Alternative reactions such as aromatic hydroxylation were also tested but found to be high in energy, while aliphatic hydroxylation is predicted to be the favored pathway.

Results and Discussion

We created cluster models based on the first- and second-coordination sphere of the AAD active site and substrate-binding pocket obtained from a molecular dynamics simulation on the crystal structure coordinates (Supporting Information). Cluster models have been used extensively for calculating the reaction mechanisms of heme and nonheme iron enzymes.[19] Generally, they include the oxidant and substrate and their direct environments with second-coordination sphere residues that interact through hydrogen-bonding, steric and charge-dipole interactions. Recent studies on cluster models showed that the second-coordination sphere is critical in the description of reaction selectivities, whereby small model complexes or QM/MM with a small QM region often predict wrong kinetics and product distributions when essential substrate-protein interactions are missing in the model.[19de] Large cluster models with more than 200 atoms as calculated with density functional theory often reproduce substrate binding and positioning in enzyme active sites well and have shown to reproduce experimental rate constants and selectivities.[19af] Consequently, they are the method of choice for enzymatic reaction mechanisms.

Our model (Figure 2) is based on the 5BKB pdb file,[16,17] and converted into the iron(IV)-oxo oxidant in the catalytic cycle of AAD by replacement of the metal ion in the pdb with an iron(IV)-oxo group with the oxygen atom trans to methylimidazole for

His_{270}, and with bound propionate instead the succinate (Succ). Furthermore, a large chain of twelve amino acid residues (Arg_{104} until Phe_{116}) that circumvents the oxidant and donates two ligands (His_{111} and Asp_{113}) to iron was included in the model. An additional eight protein residues were taken as part of the model, which describe the shape of the substrate-binding pocket through mostly aliphatic residues (Val_{80}, Pro_{81}, Leu_{82}, Leu_{83}, Val_{220}) and a Tyr residue (Tyr_{221}) that hydrogen bonds to the carboxylate group of the substrate. The model has two water molecules that form hydrogen-bonding interactions with the phenol group of Tyr_{221} and the alcohol group of Ser_{114} located in the vicinity of the substrate carboxylate group. Note that the pdb file contains **SP** as the substrate, which was manually replaced by **2,4-D**. The cluster model has 337 atoms and was calculated in the triplet and quintet spin states. In addition, we created iron(IV)-oxo cluster models with bound **SP** (^{5}**Re**$_B$) and one with bound **RP** (^{5}**Re**$_C$) by manually replacing one of the hydrogen atoms of the substrate with a methyl group.

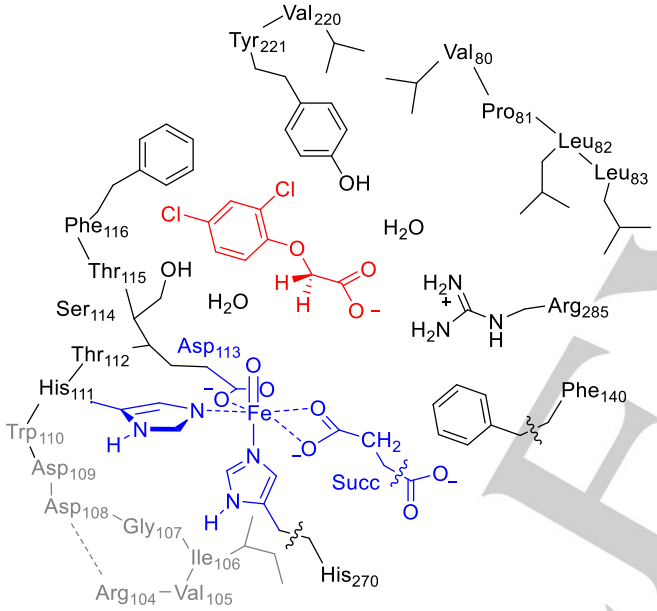

Figure 2. AAD model with **2,4-D** bound as studied in this work. Wiggly lines represent where bonds were cut and where link (hydrogen) atoms were added.

We created two substrate bound reactant structures with **2,4-D** bound, namely **Re**$_{A1}$ and **Re**$_{A2}$ that have the substrate in a different orientation. Both reactant complexes were geometry optimized in Gaussian without constraints in the triplet and quintet spin states. The unconstraint geometry optimizations did not divert the structure dramatically from the starting crystal structure coordinates and an overlay puts most atoms in similar positions (Figure S4, Supporting Information). Structure ^{5}**Re**$_{A2}$ is lower in energy than ^{5}**Re**$_{A1}$ by ΔE+ZPE = 2.8 kcal mol^{-1} (ZPE stands for zero-point energy) and as such the two substrate orientations are likely to exist alongside each other. The triplet spin reactants ^{3}**Re**$_{A1}$ and ^{3}**Re**$_{A2}$; on the other hand, are ΔE+ZPE = 15.3 and 16.4 kcal mol^{-1} higher in energy than the lowest energy quintet spin state structure ^{5}**Re**$_{A2}$. The spin state ordering does not change when a different density functional theory method or basis set is used in the calculations (see Supporting Information) or through the addition of solvent or dispersion corrections. The AAD enzyme; therefore, is expected to have an iron(IV)-oxo intermediate in its catalytic cycle with a quintet spin ground state while the triplet spin conformers will play little role of importance. Our calculated spin-state ordering is in agreement with previous calculations on iron(IV)-oxo intermediates of analogous nonheme iron dioxygenases and biomimetic model complexes,[20,21] that also found a quintet spin state for trigonal bipyramidal iron coordination. In addition, experimental work on nonheme iron enzymes characterized these systems as quintet spin ground states using electron paramagnetic resonance measurements.[11,22] Often in biomimetic iron(IV)-oxo complexes the triplet and quintet spin states are close in energy and the first-coordination sphere orientation determines what the lowest energy spin state is. In particular, in complexes with the metal in trigonal bipyramidal symmetry often the structure is stabilized a high-spin state, while in octahedral symmetry the triplet spin state is the ground state. Therefore, our calculated spin-state-ordering fits the pattern seen in nonheme iron dioxygenases and matches experiment well.[20,22]

Optimized geometries of the lowest energy quintet spin reactant structures of models ^{5}**Re**$_{A1}$ and ^{5}**Re**$_{A2}$ are shown in Figure 3. The two reactant complexes have similar first-coordination sphere interactions with almost identical Fe–O and Fe–N(His_{270}) interactions that are found within 0.001 Å of each other. An overlay (right-hand-side of Figure 3) of ^{5}**Re**$_{A1}$ and ^{5}**Re**$_{A2}$ shows that also the second-coordination sphere is virtually in the same position and little changes have incurred when the substrate was reoriented. Therefore, the enzyme is highly rigid and substrate and oxidant bind neatly into the active site, but there is space for multiple substrate orientations. In both structures the carboxylate group of the substrate forms hydrogen bonding interactions with a peptide amide group (of Ser_{114}) as well as with the guanidinium group of Arg_{285}. The other NH_2 group of Arg_{285} has hydrogen bonding interactions with the carboxylate groups of succinate and Asp_{113} of the first-coordination sphere. The main difference between the substrate positioning in ^{5}**Re**$_{A1}$ and ^{5}**Re**$_{A2}$ is related to the aliphatic CH_2 group. Thus, the pro-*S* C–H bond in ^{5}**Re**$_{A1}$ is at a distance of 2.626 Å of the iron(IV)-oxo, while the pro-*R* C–H bond is much further away at 4.297 Å. By contrast, in ^{5}**Re**$_{A2}$ both pro-*R* and pro-*S* are at large distances from the iron(IV)-oxo species, namely at 4.169 and 5.764 Å, respectively. Therefore, despite the fact that ^{5}**Re**$_{A2}$ is the lower energy isomer, the substrate orientation is lesser favorable for aliphatic C–H abstraction than in ^{5}**Re**$_{A1}$ and hence may be lesser reactive. Moreover, in ^{5}**Re**$_{A2}$ the *ortho*-carbon atom of the phenyl ring is at a shorter distance of 3.265 Å (3.287 Å in ^{5}**Re**$_{A1}$). Based on these geometries; therefore, it is not clear how the substrate will react with oxidant and consequently we tested aliphatic hydroxylation at the pro-*R* and pro-*S* positions of the substrate as well as aromatic hydroxylation of the *ortho*-position.

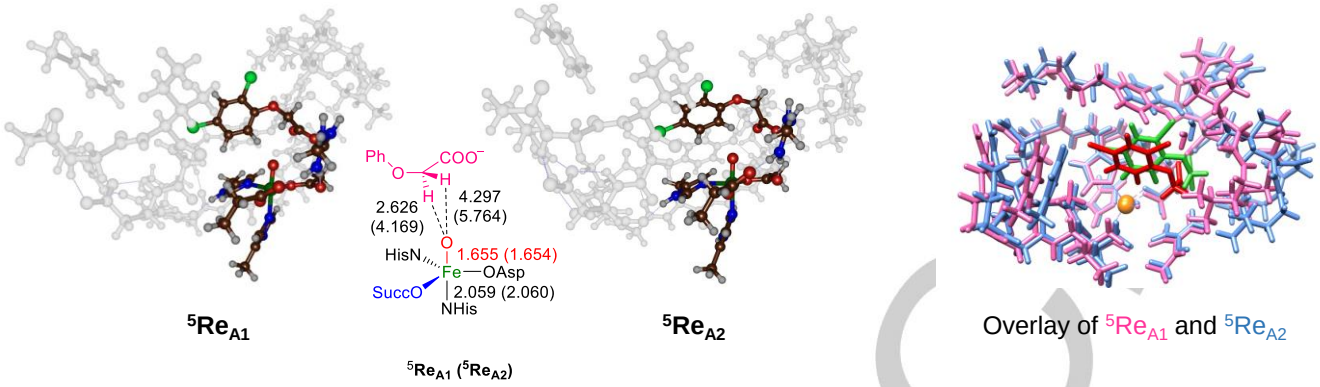

Figure 3. Optimized geometries of quintet spin reactant complexes with substrate in position A1 or A2. Bond lengths are in angstroms and the overlay of the two structures gives ^{5}**Re**$_{A1}$ in purple (substrate in red) and ^{5}**Re**$_{A2}$ in light blue (substrate in green).

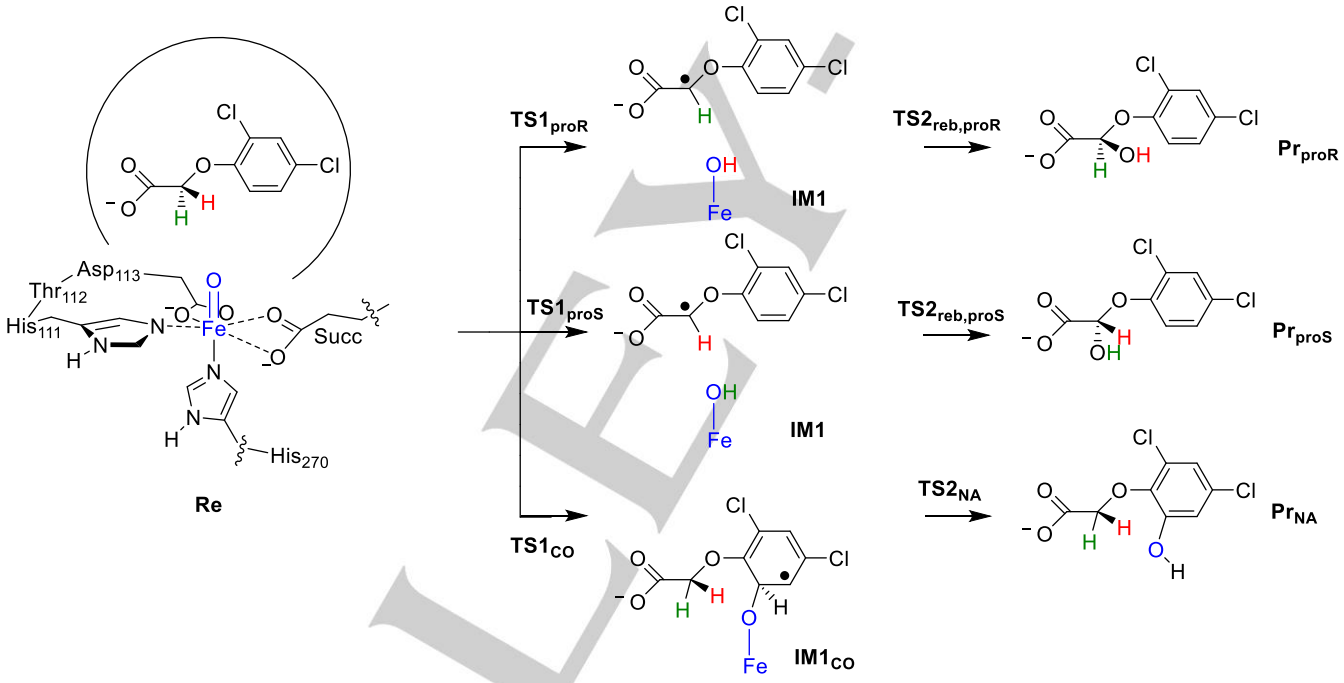

Scheme 2. Reaction mechanisms calculated for substrate activation by AAD with definition of the labels of the structures.

Next, we explored the reaction mechanisms leading to three possible products, namely pro-*R* and pro-*S* hydroxylation of the C^2-position and *ortho*-aromatic hydroxylation of **2,4-D**. Details of the mechanisms and the individual steps considered are shown in Scheme 2. The aliphatic hydroxylation starts with a hydrogen atom abstraction of the pro-*R* or pro-*S* C–H bond of the substrate via transition states **TS1**$_{proR}$ and **TS1**$_{proS}$, respectively, and relax to an iron(III)-hydroxo radical intermediate **IM1**. An OH rebound step via **TS2**$_{reb,proR}$ or **TS2**$_{reb,proS}$ gives either the *R*-2-hydroxy-**2,4-D** (**Pr**$_{proR}$) or *S*-2-hydroxy-**2,4-D** (**Pr**$_{proS}$) products. As the *ortho*-carbon atom of the phenyl ring is close in position to the iron(IV)-oxo species in both reactants complexes, we also attempted a nucleophilic pathway, where an addition complex (**IM1**$_{CO}$) is formed after a C–O bond formation transition state (**TS1**$_{CO}$). An internal hydrogen atom transfer from the *ipso*-C–H group to the oxo via transition state **TS2**$_{NA}$ gives the phenol product (**Pr**$_{NA}$).

Let us start with a discussion on the aliphatic hydroxylation of **2,4-D** leading to *R*- and *S*-C^2-hydroxylated products. Experimental studies failed to trap and characterize the singly hydroxylated species and as such it is not known if the enzyme reacts enantioselectively on **2,4-D**. Although we located two reactant complexes, ^{5}**Re**$_{A1}$ and ^{5}**Re**$_{A2}$, both connect to the same hydrogen atom abstraction transition states for hydrogen atom abstraction from the *pro-R* and *pro-S* C^2–H positions.

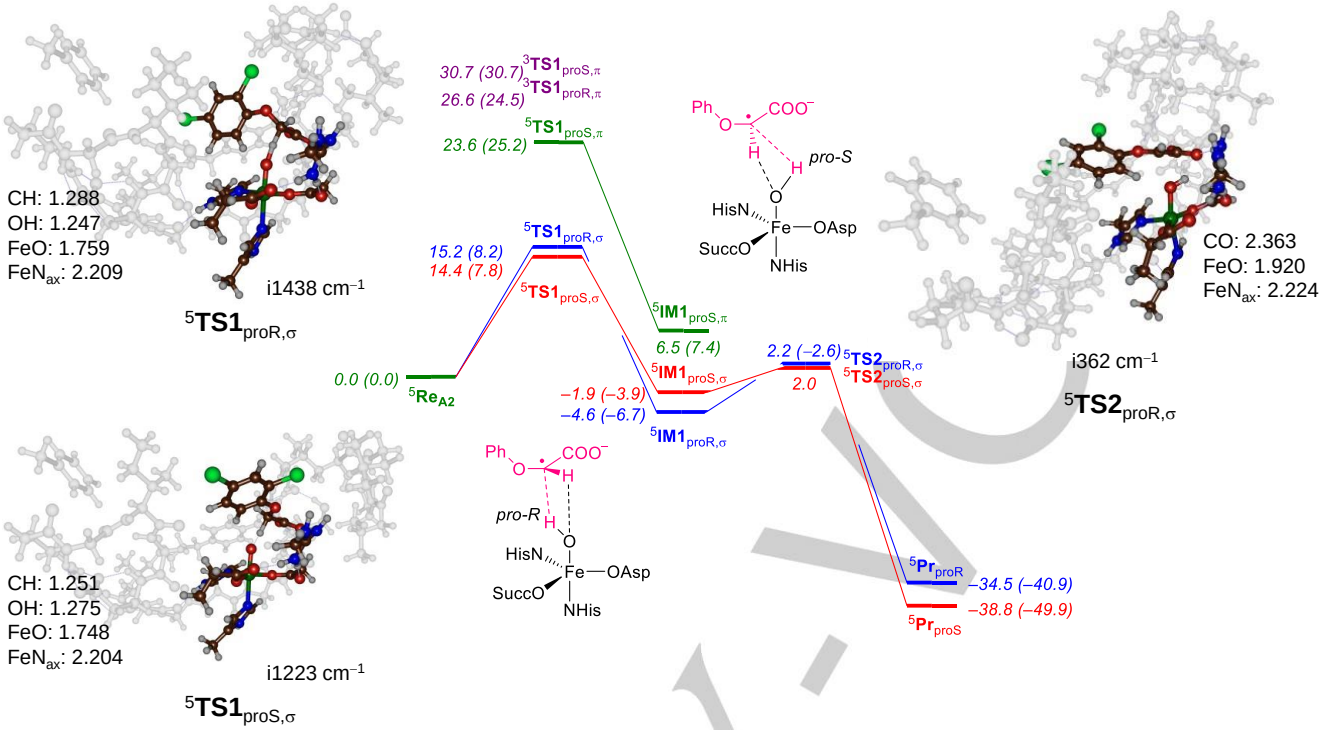

Figure 4. DFT calculated potential energy profile for **2,4-D** hydroxylation at the *pro-R* and *pro-S* positions for an AAD cluster model. Energies are in kcal mol^{-1} and are obtained at UB3LYP/BS2//UB3LYP/BS1+ZPE level of theory while values in parenthesis have dispersion corrections included. Optimized geometries give bond lengths in angstroms and the imaginary frequency in cm^{-1}.

We located transition states on the quintet spin state surface for hydrogen atom abstraction from the *pro-R* and *pro-S* positions of **2,4-D**. The hydrogen atom abstraction transition state for the *pro-R* hydrogen abstraction (^{5}**TS1**$_{proR,\sigma}$) has a barrier of ΔE+ZPE = 15.2 kcal mol^{-1}. On the other hand, the *pro-S* hydrogen atom abstraction transition state (^{5}**TS1**$_{proS,\sigma}$) is ΔE+ZPE = 14.4 kcal mol^{-1} above the reactants complex. Therefore, the calculations predict the *pro-R* and *pro-S* hydrogen atom abstraction transition states to be in a close window within 1 kcal mol^{-1} with a small preference for the *pro-S* C^2–H hydrogen atom abstraction. The ordering does not change when dispersion, thermal or entropic corrections are added to the energies.

Optimized geometries of the transition states are shown in Figure 4 as well. The *pro-R* hydrogen atom abstraction transition state is relatively central with C–H and O–H distances that are of similar magnitude: r(C–H) = 1.288 Å, r(O–H) = 1.247 Å, while these values are 1.251 and 1.275 Å for ^{5}**TS1**$_{proS,\sigma}$, respectively. The two hydrogen atom abstraction transition states both have a large imaginary frequency of i1438 cm^{-1} (*pro-R*) and i1223 cm^{-1} (*pro-S*), which will result in a significant tunneling contribution and a large kinetic isotope effect upon replacement of the hydrogen atom with deuterium. Indeed, our calculated kinetic isotope effects (Supporting Information Table S27) predicts the free energy of activation to increase by more than 2 kcal mol^{-1} leading to KIE values well over 10 with empirical tunneling corrections included. As such the structures are functionally similar in geometry as well as energy.

The Fe–O distances in the hydrogen atom transition states have elongated from 1.655 Å in ^{5}**Re**$_{A1}$ (Figure 3) to 1.759 Å in ^{5}**TS1**$_{proR,\sigma}$ and 1.748 Å in ^{5}**TS1**$_{proS,\sigma}$ (Figure 4) as expected from the electron transfer from the substrate into the σ^*_{z2} orbital along the Fe–O axis. Thus, the reactant structure has a quintet spin configuration with $\pi^*_{xy}{}^1$ $\pi^*_{xz}{}^1$ $\pi^*_{yz}{}^1$ $\sigma^*_{x2\text{-}y2}{}^1$. These orbitals represent the antibonding interactions of the metal 3d orbitals with first-coordination sphere ligands, whereby the z-axis is taken along the molecular Fe–O bond. After hydrogen atom transfer, a radical intermediate is formed (^{5}**IM1**$_\sigma$) with electronic configuration of $\pi^*_{xy}{}^1$ $\pi^*_{xz}{}^1$ $\pi^*_{yz}{}^1$ $\sigma^*_{x2\text{-}y2}{}^1$ $\sigma^*_{z2}{}^1$ $\pi_{Sub}{}^1$. The metal type orbitals are singly occupied with a α-spin electron, while the substrate radical has a β-spin electron in orbital π_{Sub}.

For a number of radical intermediate structures we attempted to locate the alternative π-type intermediate (^{5}**IM1**$_\pi$) with configuration $\pi^*_{xy}{}^2$ $\pi^*_{xz}{}^1$ $\pi^*_{yz}{}^1$ $\sigma^*_{x2\text{-}y2}{}^1$ $\pi_{Sub}{}^1$, whereby all unpaired electrons are up-spin. For the *pro-S* hydrogen atom abstraction pathway, we located both ^{5}**IM1**$_{proS,\sigma}$ and ^{5}**IM1**$_{proS,\pi}$ states as well as the two transition states leading to these radical complexes, namely ^{5}**TS1**$_{proS,\sigma}$ and ^{5}**TS1**$_{proS,\pi}$, and found the σ-type transition state and intermediate the lowest in energy by at least 8 kcal mol^{-1}. In particular, the ^{5}**TS1**$_{proS,\pi}$ was 23.6 kcal mol^{-1} above the energy of the reactants and consequently well higher in energy than the σ-type transition states and hence the π-pathway will not be able to compete with the σ-pathway. This result matches previous calculations on the σ- versus π-configuration in iron(III)-hydroxo complexes.[23] Although the triplet spin reactants were well above the quintet spin reactants, we calculated and optimized the hydrogen atom abstraction transition states for the *pro-R* and *pro-S* positions as well.

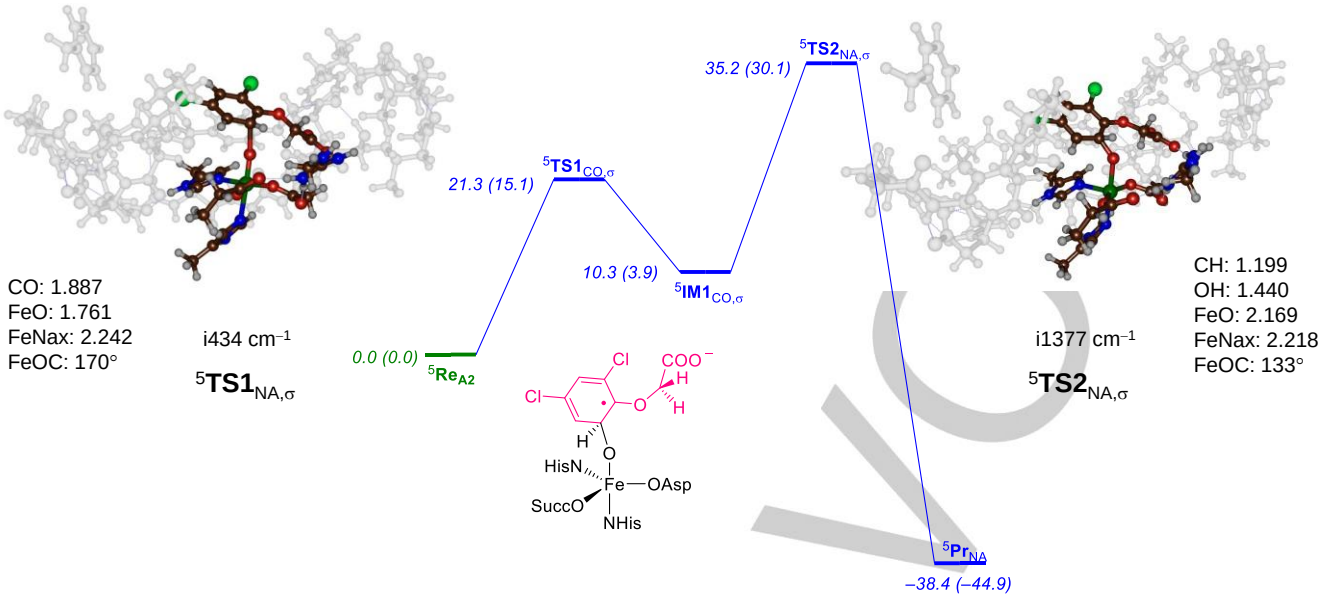

Figure 5. DFT calculated potential energy profile for aromatic hydroxylation of **2,4-D** hydroxylation by an AAD cluster model. Energies are in kcal mol^{-1} and are obtained at UB3LYP/BS2//UB3LYP/BS1+ZPE level of theory while values in parenthesis have dispersion corrections included. Optimized geometries give bond lengths in angstroms and the imaginary frequency in cm^{-1}.

These transition states are very high in energy, 26.6 and 30.7 kcal mol^{-1} respectively, and consequently, the triplet spin state will play little role in the substrate activation mechanism.

After the radical intermediate an OH rebound transition state leads to the *R*- and *S*-hydroxy products. The ^{5}**TS2**$_{proR,\sigma}$ and ^{5}**TS2**$_{proS,\sigma}$ transition states are of the same level of energy and are much smaller than the hydrogen atom abstraction, which will be rate-determining. The ^{5}**TS2**$_{proR,\sigma}$ structure has a long C–O bond of 2.363 Å and hence is an early transition state. Previous DFT calculations on OH rebound reactions gave similar structures with long C–O bonds and elongated Fe–O bonds.[24] The imaginary frequency for the OH rebound transition state is i362 cm^{-1} and shows a C–O stretch vibration as expected.

As the substrate contains an aromatic ring, we considered aromatic hydroxylation at the *ortho*-position with respect to the ether bond and studied this pathway for the model A2 reactant structure. The obtained energy profile and optimized geometries of the transition states along the aromatic hydroxylation pathway are shown in Figure 5. The initial C–O bond formation transition state is relatively high in energy (ΔE+ZPE = 21.3 kcal mol^{-1}) and is well higher in energy than the hydrogen atom abstraction barriers shown in Figure 4. Structurally, the nucleophilic transition state (^{5}**TS1**$_{CO,\sigma}$) is relatively linear with a Fe–O–C angle of 170° and long C–O and Fe–O bonds of 1.887 and 1.761 Å. The transition state has an imaginary frequency of i434 cm^{-1} corresponding to a C–O stretch vibration. This magnitude of the imaginary frequency is typical for aromatic hydroxylation transition state that typically have a broad potential energy surface with imaginary frequencies below i500 cm^{-1}.[25]

After the transition state the system relaxes to a radical intermediate with $\pi^*_{xy}{}^1$ $\pi^*_{xz}{}^1$ $\pi^*_{yz}{}^1$ $\sigma^*_{x2\text{-}y2}{}^1$ $\sigma^*_{z2}{}^1$ $\pi_{Sub}{}^1$ configuration, i.e. the $^5\sigma$-pathway as discussed above in aliphatic hydroxylation. The radical intermediate ^{5}**IM1**$_{CO,\sigma}$; however, is less stable than the reactants complex by ΔE+ZPE = 10.3 kcal mol^{-1}, which means it has a relatively small barrier for the reverse reaction leading back to the reactants complex. Furthermore, the subsequent hydrogen atom transfer from the *ipso*-position to the oxygen atom has a high barrier of 35.2 kcal mol^{-1}. This is a relatively high barrier that will make the alternative aromatic hydroxylation process unlikely at room temperature. In previous studies such as the cytochromes P450, it was shown that this step is assisted by a basic residue in the substrate binding pocket, such as a pyrrole-heme nitrogen atom that would act as a springboard and shuttle the proton from the *ipso*-position to the oxygen atom.[25a] In the structure of AAD; however, no proton acceptor group is available nearby the *ipso*-proton and hence a proton shuttle mechanism is not feasible here. As a consequence only a direct hydrogen atom transfer is possible, which is high in energy. It is clear that the substrate binding pocket in AAD is not accommodated for an aromatic hydroxylation process. Nevertheless, the overall aromatic hydroxylation reaction is highly exothermic and the product complex is more stable than reactants by 38.4 kcal mol^{-1}, but due to slow kinetics it may not be a possible product.

Next, we explored the reactivity of alternative substrates in the AAD model and considered the enzyme inhibitors *R*- and *S*-2-(2,4-dichlorophenoxy)propanoate (molecules **RP** and **SP**). To this end we took the ^{5}**Re**$_{A1}$ optimized geometry and manually replaced **2,4-D** with either **SP** or **RP** to obtain the model **B** and **C** reactant complexes: ^{5}**Re**$_B$ and ^{5}**Re**$_C$. Figure 6 shows details of the aliphatic hydroxylation pathways of the two alternative substrates. Interestingly, both models give similar hydrogen atom abstraction barriers, i.e. 16.2 kcal mol^{-1} for ^{5}**TS1**$_{proR,B,\sigma}$ and 16.4 kcal mol^{-1} for ^{5}**TS1**$_{proS,C,\sigma}$.

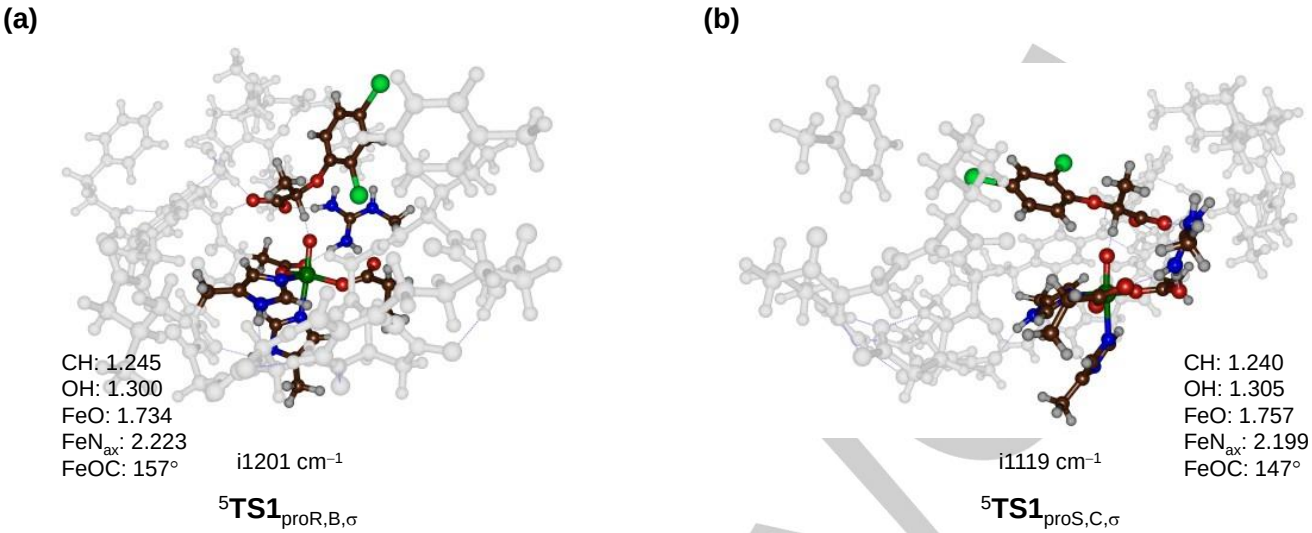

	^{5}TS1$_\sigma$	^{5}IM1$_\sigma$	^{5}TS2$_\sigma$	^{5}Pr
Model **B**, substrate **SP**	16.2	-4.9	15.7	-37.4
Model **C**, substrate **RP**	16.4	-3.9	1.8	-33.8

Figure 6. Activation of inhibitors **SP** and **RP** by the iron(IV)-oxo model complex of AAD. Energies are in kcal mol^{-1} and are obtained at UB3LYP/BS2//UB3LYP/BS1+ZPE level of theory. Optimized geometries give bond lengths in angstroms and the imaginary frequency in cm^{-1}.

These barriers are somewhat higher in energy than those found for **2,4-D** and show that the second-coordination sphere makes the hydrogen atom abstraction more difficult. The raise in hydrogen atom abstraction barriers from **2,4-D** to **SP**/**RP** is surprising as in **SP** and **RP** and tertiary C–H bond is broken, whereas in **2,4-D** a secondary C–H bond is broken. Usually, tertiary C–H bond strengths are weaker than secondary C–H bond strengths and lead to lower hydrogen atom abstraction barriers. Therefore, a lower energy hydrogen atom abstraction barrier would be expected for **SP** and **RP** than for **2,4-D**, which clearly is not the case in AAD. Consequently, the substrate binding pocket may affect substrate positioning and hamper the hydrogen atom abstraction barriers for **RP** and **SP**.

Structurally, the hydrogen atom abstraction transition states from **RP** and **SP** by AAD are indeed very similar with C–H and O–H distances within 0.005 Å. The ^{5}**TS1**$_{proR,B,\sigma}$ is slightly more upright with an Fe–O–C angle of 157°, while it is only 147° for ^{5}**TS1**$_{proS,C,\sigma}$. Both transition states have a large imaginary frequency for hydrogen atom transfer with magnitude of i1201 cm^{-1} for ^{5}**TS1**$_{proR,B,\sigma}$ and i1119 cm^{-1} for ^{5}**TS1**$_{proS,C,\sigma}$. These values indicate that the hydrogen atom abstraction will undergo significant amount of tunneling and will experience a large kinetic isotope effect when the transferring hydrogen is replaced by deuterium.

After the hydrogen atom abstraction from either **RP** or **SP** a radical intermediate is formed. However, despite the fact that OH rebound has a relatively small barrier for **RP** (ΔE+ZPE = 6.7 kcal mol^{-1} above ^{5}**IM1**$_{C,\sigma}$) the barrier for rebound for **SP** is much larger, namely 20.6 kcal mol^{-1} above the radical intermediate ^{5}**IM1**$_{B,\sigma}$). This implies that radical rebound will be rate-determining for substrate **SP** and due to the high barrier the reaction will be slow. On the other hand, for **RP** the rebound is lower and the rate-determining step will be hydrogen atom abstraction with significantly lower barrier than OH rebound for substrate **SP**. Therefore, the two stereoisomers **RP** and **SP** will react differently in AAD enzymes and different product distributions will be obtained. As **RP** and **SP** have the same number of atoms, we analyzed the substrate binding energies into the substrate binding pocket by comparing the relative energies of ^{5}**Re**$_{B,SP}$ and ^{5}**Re**$_{C,RP}$. Thus, ^{5}**Re**$_{C,RP}$ is lower in energy than ^{5}**Re**$_{B,SP}$ by 3.4 kcal mol^{-1}. As such, the **RP** inhibitor will be stronger bound than **SP** in the AAD substrate-binding pocket and consequently, product release will be more energetic for **RP** than **SP**. Therefore, there are differences in stability, reactivity and rebound barriers for the reactions of AAD with **RP** and **SP**.

To understand the differences in kinetics between **2,4-D** and **RP**/**SP**, we calculated homolytic bond dissociation energies (BDEs). Firstly, we took isolated substrates and calculated their geometry and energy in the gas-phase. Subsequently, the structure was recalculated with one hydrogen atom removed in the doublet spin state. Together with the energy of a hydrogen atom, the BDE was calculated for the *pro-R* and *pro-S* C^2–H bonds of **2,4-D** as well as the C–H bonds in **RP** and **SP**. In the gas-phase, not surprisingly, the tertiary C–H bonds in **RP** and **SP** are the weakest at 87.3 kcal mol^{-1}, while the secondary C^2–H bonds in **2,4-D** both have a BDE = 90.5 kcal mol^{-1}. Generally, hydrogen atom abstraction barriers correlate with the strength of the C–H bond that is broken and hence a lower barrier for **RP** and **SP** would be expected than for **2,4-D**.

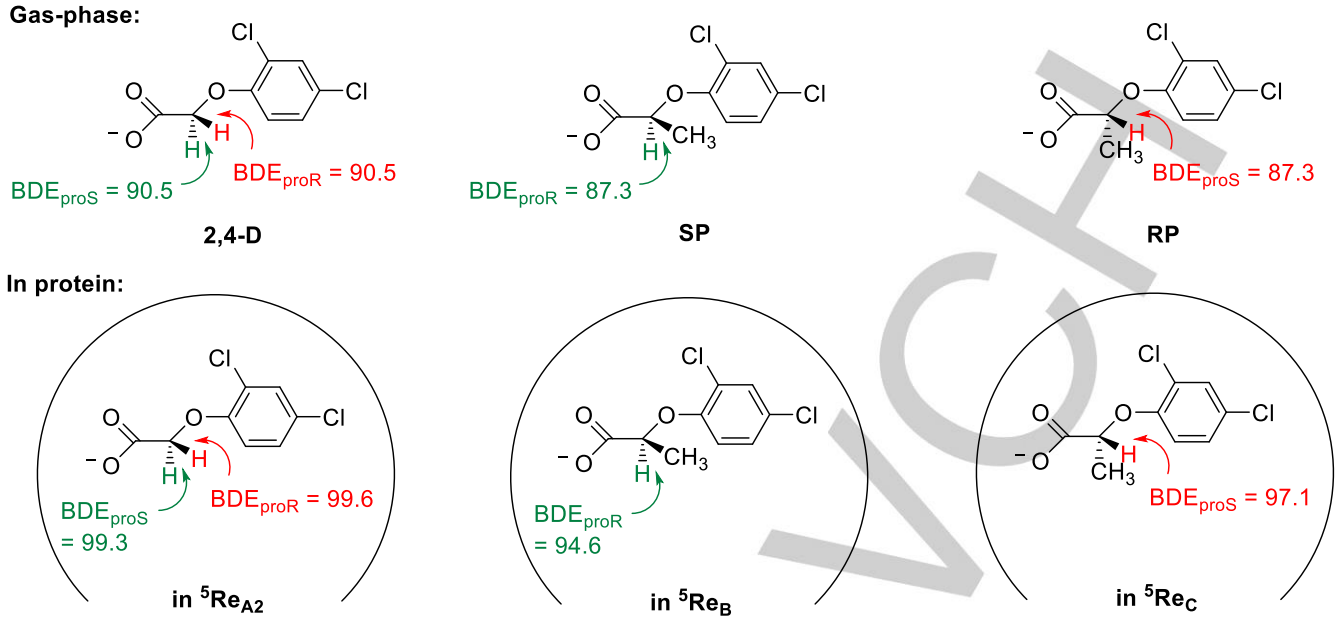

Figure 7. Calculated (UB3LYP/BS2) values for substrate BDEs in the gas phase (top) or inside a protein environment for the substrate-bound reactant complexes. Energies contain ZPE and are in kcal mol^{-1} for the abstraction of a hydrogen atom.

The hydrogen atom abstraction barriers, however, do not follow the trend in BDE values and we find lower hydrogen atom abstraction barriers from the C^2–H position for **2,4-D** as a substrate than **RP** or **SP**. Therefore, the interactions of the protein and steric restraints of the substrate-binding pocket must affect the kinetics.

To find out how and if the protein affects the BDE values through long-range electrostatic interactions, we took the structures of ^{5}**Re**$_{A2}$, ^{5}**Re**$_B$ and ^{5}**Re**$_C$ and did a single point energy calculation at B3LYP/BS2 for a sextet spin state with one hydrogen atom removed from the C^2–H position of substrate. We then calculated the substrate diabatic BDE values inside the protein matrix and the results are shown at the bottom of Figure 7. As can be seen, the BDE values of **2,4-D** change inside the protein and both *pro-R* and *pro-S* C^2–H bonds are stronger with values of 99.6 and 99.3 kcal mol^{-1}. Despite this, the calculations find that there should not be a selectivity for hydrogen atom abstraction from the C^2–H bond with almost equal bond energies. This is indeed what the potential energy landscapes above show. As these values are close in energy similar hydrogen atom abstraction barriers are expected, which is indeed seen from the full transition state optimizations from Figure 4.

Similarly to the BDEs of **2,4-D** inside the protein, also the C^2–H BDEs for **SP** and **RP** were evaluated from the reactant complexes ^{5}**Re**$_B$ and ^{5}**Re**$_C$. In both cases the C–H bond strength goes up by about 10 kcal mol^{-1} with respect to the gas-phase BDE. Moreover, the C^2–H BDEs for **SP** and **RP** inside the protein are both lower in energy than the ones for **2,4-D**. This would mean a lower hydrogen atom abstraction for **SP** or **RP** as a substrate compared to **2,4-D**. However, the fully characterized transition states show slightly higher energy barriers for **SP** and **RP** (16.2 and 16.4 kcal mol^{-1}) as compared to those from **2,4-D** (*pro-R* at 15.2 kcal mol^{-1} and *pro-S* at 14.4 kcal mol^{-1}). Therefore, steric restraints of substrate approach rather than long-range electrostatic contributions affect the kinetics of substrate activation in AAD.

Conclusion

The work described in this paper is focused on the binding and activation of herbicide molecules to the nonheme iron enzyme AAD. Cluster models with **2,4-D**, **RP** and **SP** bound in the AAD binding pocket with iron(IV)-oxo present were generated and the substrate hydroxylation pathways studied with density functional theory methods. The work shows that all three substrate can bind into the active site and react through C^2–H hydroxylation, which is identified as the initial product of the AAD reaction with substrate. The reaction pathways are stepwise via a radical intermediate and with a rate-determining hydrogen atom abstraction step. The *pro-R* and *pro-S* hydrogen atom abstraction barriers are close in energy and so is the subsequent OH rebound. Consequently, the DFT calculations predict a mixture of *R*- and *S*-hydroxy-**2,4-D** as products. The alternative aromatic hydroxylation was also studied but found to be high in energy mostly due to the absence of a proton shuttle acceptor that can relay a proton from the aromatic ring to the phenol group. Subsequently, we studied **RP** and **SP** hydroxylation by AAD and show that the hydrogen atom abstraction barriers – against expectation based on BDE values – are higher in energy than those for **2,4-D**. Despite the slower hydrogen atom abstraction step, both substrates can be activated by AAD, fit the substrate binding pocket well and should give hydroxylated products efficiently. Although there may be differences in overall reaction rate due to major differences in OH rebound barrier for the two stereo-isomers as a result of the substrate binding pocket interactions that slow down the OH rebound step for **SP**. Overall, the work shows that

2,4-D and analogous substrates can be biodegraded by AAD enzymes efficiently and detoxified. Therefore, this should give ample applications of AAD in biotechnology and agriculture.

Experimental Section

Model Set-Up. A cluster model was designed based on the crystal structure coordinates of the substrate and α-ketoglutarate bound form of AAD-1 reported by Nair et al[16] and deposited as the 5BKB pdb file at the protein databank.[17] This is an engineered protein structure saturated with manganese(II) rather than iron(II). Subsequently, the manganese(II)-α-ketoglutarate group in the pdb was replaced by iron(IV)-oxo-succinate. We selected the residues from chain A and added hydrogen atoms in Chimera at pH = 7.3.[26] A molecular dynamics (MD) simulation was performed (Supporting Information) and shows that the structure is highly rigid and has a tight substrate binding pocket.

Next, we created a cluster model based on the last point of the MD simulation. We took the iron(IV)-oxo(succinate) and abbreviated succinate in our model to propionate. In the model (Figure 2) the axial histidine residue (His_{270}) was truncated to methylimidazole, while the other protein ligands of the metal were part of the peptide chain Arg_{104}-Val_{105}-Ile_{106}-Gly_{107}-Asp_{108}-Asp_{109}-Trp_{110}-His_{111}-Thr_{112}-Asp_{113}-Ser_{114}-Thr_{115}-Phe_{116} with Val_{105}, Trp_{110}, Thr_{112} and Thr_{115} shortened to a Gly residue. In addition, part of the substrate binding pocket was included in the model, namely the chain Val_{80}-Pro_{81}-Leu_{82}-Leu_{83} and the peptide dimer Val_{220}-Tyr_{221}. The Phe_{140} and Arg_{285} side chains were abbreviated to toluene and methylguanidine. The overall model is shown in Figure 2 and had a total of 337 atoms and has overall charge −1. We calculated this system in the lowest lying triplet and quintet spin states. The inhibitor models were started from the optimized geometries of the ^{5}**Re**$_{A2}$ structures, where substrate **2,4-D** was manually replaced to **RP** or **SP** by replacing one of the C^2–H groups to C^2–CH_3.

Computational Approach. The *Gaussian*-09 software package was used for all quantum chemical calculations discussed here.[27] Following our previous experience with cluster models of nonheme iron dioxygenases,[28] we utilized the unrestricted B3LYP density functional method in combination with a LANL2DZ (with electron core potential) on iron and 6-31G on the rest of the atoms: basis set BS1.[29,30] To correct the energetics, single point calculations with the LACV3P+ (with electron core potential) on iron and 6-311+G* on the rest of the atoms were performed. The latter set of calculations included a continuum polarized conductor model (CPCM) with a dielectric constant mimicking chlorobenzene.[31] We ran some test calculations with the SMD solvent model and find quantitatively the same trends as with CPCM, see Supporting Information for details.

To validate the methods and models a series of test calculations on the rate-determining steps were performed using the PBE0/BS2 and B3LYP-D3/BS2 methods.[29,32,33] These calculations predicted the same trends in spin-state-ordering and chemoselectivity and hence did not change the conclusions. Frequency calculations were performed on all local minima and transition states and it was confirmed that local minima had real frequencies only, while the transition states had a single imaginary mode for the correct vibration along the reaction coordinate. The amount of spin contamination in the optimized geometries was verified for each structure and the S^2 values for the triplet spin structures are close to the ideal value of 2, while those for the quintet spin structures are close to the ideal value of 6.

Acknowledgements

The Punjab Education Endowment Fund (PEEF) in Pakistan is acknowledged for a PhD scholarship to HSA.

Keywords: enzyme mechanism • nonheme iron • hydroxylation • density functional theory • inorganic reaction mechanisms

References

[1] F. Islam, J. Wang, M. A. Farooq, M. S.S. Khan, L. Xu, J. Zhu, M. Zhao, S. Muños, Q. X. Li, W. Zhou, *Environm Intern*. **2018**, *111*, 332-351.

[2] a) R. R. Fulthorpe, C. McGowan, O. V. Maltseva, W. E. Holben, J. M. Tiedje, *Appl. Environm. Microbiol*. **1995**, *61*, 3274-3281; b) T. Paszko, P. Muszyński, M. Materska, M. Bojanowska, M. Kostecka, I. Jackowska, *Environ. Toxicol. Chem*. **2016**, *35*, 271-286; c) D. Chen, S. Wu, H. Xue, J. Jiang, *Int. Biodeterior. Biodegrad*. **2020**, *146*, 104822; d) N. V. Coleman, D. J. Rich, F. H. M. Tang, W. Vervoort, F. Maggi, *Environ. Sci. Technol*. **2020**, *54*, 10399-10410; e) K. Fukui, K.-i. Hayashi, *Plant Cell Physiol*. **2018**, *59*, 1500-1510.

[3] D. C. Ruen, E. F. Scherder, S. C. Ditmarsen, P. L. Prasifka, J. M. Ellis, D. M. Simpson, C. A. Gallup, B. W. Hopkins, *Weed Technol*. **2017**, *31*, 217-224.

[4] T. R. Wright, G. Shan, T. A. Walsh, J. M. Lira, C. Cui, P. Song, M. Zhuang, N. L. Arnold, G. Lin, K. Yau, S. M. Russell, R. M. Cicchillo, M. A. Peterson, D. M. Simpson, N. Zhou, J. Ponsamuel, Z. Zhang, *Proc. Natl. Acad. Sci. USA* **2010**, *107*, 20240-20245.

[5] a) Y. Song, *J. Integrat. Plant Biol*. **2014**, *56*, 106-113; b) M. A. Peterson, S. A. McMaster, D. E. Riechers, J. Skelton, P. W. Stahlman, *Weed Technol*. **2016**, *30*, 303-345; c) J. Zhou, K. Liu, F. Xin, J. Ma, N. Xu, W. Zhang, Y. Fang, M. Jiang, W. Dong, *World J. Microbiol. Biotechnol*. **2018**, *34*, 117-125; d) M. P. Serbent, A. M. Rebelo, A. Pinheiro, A. Giongo, L. B. Ballod Tavares, *Appl. Microbiol. Biotechnol*. **2019**, *103*, 5065-5078; e) K. Magnoli, C. Soledad Carranza, M. Eglé Aluffi, C. E. Magnoli, C. L. Barberis, *Environ. Sci. Pollut. Res*. **2020**, *27*, 38501-38512.

[6] F. Fukumori, R. P. Hausinger, *J. Bacteriol*. **1993**, *175*, 2083-2086.

[7] a) E. I. Solomon, T. C. Brunold, M. I. Davis, J. N. Kemsley, S. K. Lee, N. Lehnert, F. Neese, A. J. Skulan, Y. S. Yang, J. Zhou, *Chem. Rev*. **2000**, *100*, 235–349; b) T. D. H. Bugg, *Curr. Opin. Chem. Biol*. **2001**, *5*, 550–555; c) M. J. Ryle, R. P. Hausinger, *Curr. Opin. Chem. Biol*. **2002**, *6*, 193–201; d) M. Costas, M. P. Mehn, M. P. Jensen, L. Que Jr., *Chem. Rev*. **2004**, *104*, 939–986; e) M. M. Abu-Omar, A. Loaiza, N. Hontzeas, *Chem. Rev*. **2005**, *105*, 2227–2252; f) C. Krebs, D. G. Fujimori, C. T. Walsh, J. M. Bollinger Jr, *Acc. Chem. Res*. **2007**, *40*, 484–492; g) S. P. de Visser, D. Kumar (Eds.) *Iron-containing enzymes: Versatile catalysts of hydroxylation reactions in nature*, Royal Society of Chemistry Publishing, Cambridge (UK), 2011; h) A. R. McDonald, L. Que Jr, *Coord. Chem. Rev*. **2013**, *257*, 414–428.

[8] a) A. G. Prescott, M. D. Lloyd, *Nat. Prod. Rep*. **2000**, *17*, 367–383; b) F. Kudo, A. Miyanaga, T. Eguchi, *Nat. Prod. Rep*. **2014**, *31*, 1056–1073; c) D. Baud, P.-L. Saaidi, A. Monfleur, M. Harari, J. Cuccaro, A. Fossey, M. Besnard, A. Debard, A. Mariage, V. Pellouin, J.-L. Petit, M. Salanoubat, J. Weissenbach, V. de Berardinis, A. Zaparucha, *ChemCatChem*. **2014**, *6*, 3012–3017.

[9] a) J. H. Carter II, R. H. Du Bus, J. R. Dyer, J. C. Floyd, K. C. Rice, P. D. Shaw, *Biochemistry* **1974**, *13*, 1227–1233; b) J. Zhou, W. L. Kelly, B. O. Bachmann, M. Gunsior, C. A. Townsend, E. I. Solomon, *J. Am. Chem. Soc*. **2001**, *123*, 7388-7398; c) X. Yin, T. M. Zabriskie, *ChemBioChem*. **2004**, *5*, 1274–1277; d) V. Helmetag, S. A. Samel, M. G. Thomas, M. A. Marahiel, L.-O. Essen, *FEBS J*. **2009**, *276*, 3669–3682; e) A. J. Mitchell, N. P. Dunham, R. J. Martinie, J. A. Bergman, C. J. Pollock, K. Hu, B. D. Allen, W.-c. Chang, A. Silakov, J. M. Bollinger Jr, C. Krebs, A. K. Boal, *J. Am. Chem. Soc*. **2017**, *139*, 13830–13836; f) N. P. Dunham, A. J. Mitchell, J. M. Del Río Pantoja, C. Krebs, J. M. Bollinger Jr, A. K. Boal, *Biochemistry* **2018**, *57*, 6479–6488.

[10] a) G. D. Straganz, B. Nidetzky, *ChemBioChem*. **2006**, *7*, 1536–1548; b) C. A. Joseph, M. J. Maroney, *Chem. Commun*. **2007**, 3338–3349; c) D.

Buongiorno, G. D. Straganz, *Coord. Chem. Rev*. **2013**, *257*, 541–563; d) E. P. Tchesnokov, M. Fellner, E. Siakkou, T. Kleffmann, L. W. Martin, S. Aloi, I. L. Lamont, S. M. Wilbanks, G. N. L. Jameson, *J. Biol. Chem*. **2015**, *290*, 24424–24437.

[11] a) J. C. Price, E. W. Barr, B. Tirupati, J. M. Bollinger Jr, C. Krebs, *Biochemistry* **2003**, *42*, 7497–7508; b) D. A. Proshlyakov, T. F. Henshaw, G. R. Monterosso, M. J. Ryle, R. P. Hausinger, *J. Am. Chem. Soc*. **2004**, *126*, 1022–1023; c) P. J. Riggs-Gelasco, J. C. Price, R. B. Guyer, J. H. Brehm, E. W. Barr, J. M. Bollinger Jr, C. Krebs, *J. Am. Chem. Soc*. **2004**, *126*, 8108–8109; d) M. L. Neidig, C. D. Brown, K. M. Light, D. Galonić-Fujimori, E. M. Nolan, J. C. Price, E. W. Barr, J. M. Bollinger Jr, C. Krebs, C. T. Walsh, E. I. Solomon, *J. Am. Chem. Soc*. **2007**, *129*, 14224–14231; e) P. K. Grzyska, E. H. Appelman, R. P. Hausinger, D. A. Proshlyakov, *Proc. Natl. Acad. Sci. USA* **2010**, *107*, 3982–3987

[12] L. M. Hoffart, E. W. Barr, R. B. Guyer, J. M. Bollinger Jr, C. Krebs, *Proc. Natl. Acad. Sci. USA* **2006**, *103*, 14738–14743.

[13] a) T. A. Müller, M. I. Zavodszky, M. Feig, L. A. Kuhn, R. P. Hausinger, *Protein Science* **2006**, *15*, 1356-1368; b) J. Huang, D. Chen, J. Jiang, *Environmental Microbiol*. **2020**, *22*, 286-296; c) W. A. Peer, *Curr. Opin. Plant Biotechnol*. **2013**, *23*, 561-568.

[14] K. Nickel, M. J.-F. Suter, H.-P. E. Kohler, *J. Bacteriol*. **1997**, *179*, 6674-6679.

[15] E. J. Perkins, M. P. Gordon, O. Caceres, P. L. Lurquin, *J. Bacteriol*. **1990**, *172*, 2351-2359.

[16] J. R. Chekan, C. Ongpipattanakul, T. R. Wright, B. Zhang, J. M. Bollinger Jr, L. J. Rajakovich, C. Krebs, R. M. Cicchillo, S. K. Nair, *Proc. Natl. Acad. Sci. USA* **2019**, *116*, 13299-13304.

[17] H. M. Berman, J. Westbrook, Z. Feng, G. Gilliland, T. N. Bhat, H. Weissig, I. N. Shindyalov, P. E. Bourne, *Nucl. Acids Res*. **2000**, *28*, 235–242.

[18] a) M. A. Bhat, T. Ishida, K. Horiike, C. S. Vaidyanathan, M. Nozaki, *Arch. Biochem. Biophys*. **1993**, *300*, 738-746; b) T. Ledger, D. H. Pieper, B. González, *Appl. Environm. Microbiol*. **2006**, *72*, 2783-2792; c) C. T. Larue, M. Goley, L. Shi, A. G. Evdokimov, O. C. Sparks, C. Ellis, A. M. Wollacott, T. J. Rydel, C. E. Halls, B. Van Scoyoc, X. Fu, J. R. Nageotte, A. M. Adio, M. Zheng, E. J. Sturman, G. S. Garvey, M. J. Varagona, *Pest Manag. Sci.* **2019**, *75*, 2086–2094; d) R. Zallot, N. Oberg, J. A. Gertl, *Curr. Opin. Biotechnol*. **2021**, *69*, 77-90; e) K. Hoyerova, P. Hosek, M. Quareshy, J. Li, P. Klima, M. Kubes, A. A. Yemm, P. Neve, A. Tripathi, M. J. Bennett, R. M. Napier, *New Phytologist* **2018**, *217*, 1625-1639.

[19] a) M. R. A. Blomberg, T. Borowski, F. Himo, R.-Z. Liao, P. E. M. Siegbahn, *Chem. Rev*. **2014**, *114*, 3601–3658; b) S. P. de Visser, M. G. Quesne, B. Martin, P. Comba, U. Ryde, *Chem. Commun*. **2014**, *50*, 262–282; c) M. G. Quesne, T. Borowski, S. P. de Visser, *Chem. Eur. J*. **2016**, *22*, 2562–2581; d) X. Sheng, M. Kazemi, F. Planas, F. Himo, *ACS Catal*. **2020**, *10*, 6430–6449; e) C.-C. G. Yeh, C. Pierides, G. N. L. Jameson, S. P. de Visser, *Chem. Eur. J*. **2021**, *27*, 13793–13806; f) S. P. de Visser, Y.-T. Lin, H. S. Ali, U. K. Bagha, G. Mukherjee, C. V. Sastri, *Coord. Chem. Rev*. **2021**, *439*, 213914.

[20] a) T. Borowski, A. Bassan, P. E. M. Siegbahn, *Chem. Eur. J*. **2004**, *10*, 1031–1041; b) S. P. de Visser, *J. Am. Chem. Soc*. **2006**, *128*, 9813–9824; c) A. V. Nemukhin, I. A. Topol, R. E. Cachau, S. K. Burt, *Theor. Chem. Acc*. **2006**, *115*, 348–353; d) S. Sinnecker, N. Svensen, E. W. Barr, S. Ye, J. M. Bollinger Jr, F. Neese, C. Krebs, *J. Am. Chem. Soc*. **2007**, *129*, 6168–6179; e) E. Godfrey, C. S. Porro, S. P. de Visser, *J. Phys. Chem. A* **2008**, *112*, 2464–2468; f) H. Chen, W. Lai, J. Yao, S. Shaik, *J. Chem. Theory Comput*. **2011**, *7*, 3049–3053; g) E. A. C. Bushnell, G. B. Fortowsky, J. W. Gauld, *Inorg. Chem*. **2012**, *51*, 13351–13356; h) H. J. Kulik, C. L. Drennan, *J. Biol. Chem*. **2013**, *288*, 11233–11241; i) A. Wójcik, M. Radoń, T. Borowski, *J. Phys. Chem. A* **2016**, *120*, 1261–1274; j) S. Álvarez-Barcia, J. Kästner, *J. Phys. Chem. B* **2017**, *121*, 5347–5354; k) R. N. Manna, T. Malakar, B. Jana, A. Paul, *ACS Catal*. **2018**, *8*, 10043–10050; l) J. E. M. N. Klein, G. Knizia, *Angew. Chem. Int. Ed*. **2018**, *57*, 11913–11917; m) S. S. Chaturvedi, R. Ramanan, N. Lehnert, C. J. Schofield, T. G. Karabencheva-Christova, C. Z. Christov, *ACS Catal*. **2020**, *10*, 1195–1209; n) M. G. Quesne, R. Latifi, L. E. Gonzalez-Ovalle, D. Kumar, S. P. de Visser, *Chem. Eur. J*. **2014**, *20*, 435–446; o) H. S. Ali, R. Henchman, S. P. de Visser, *J. Phys. Chem. A* **2021**, *125*, 1720–1737.

[21] a) H. Hirao, D. Kumar, L. Que Jr, S. Shaik, *J. Am. Chem. Soc*. **2006**, 128, 8590–8606; b) I. Prat, J. S. Mathieson, M. Guëll, X. Ribas, J. M. Luis, L. Cronin, M. Costas, *Nature Chem*. **2011**, *3*, 788–793; c) R. Latifi, M. A. Sainna, E. V. Rybak-Akimova, S. P. de Visser, *Chem. Eur. J*. **2013**, *19*, 4058–4068; d) A. Ansari, A. Kaushik, G. Rajaraman, *J. Am. Chem. Soc*. **2013**, *135*, 4235–4249; e) T. Z. H. Gani, H. J. Kulik, *ACS Catal*. **2018**, *8*, 975–986; f) V. Dantignana, J. Serrano-Plana, A. Draksharapu, C. Magallón, S. Banerjee, R. Fan, I. Gamba, Y. Guo, L. Que Jr, M. Costas, A. Company, *J. Am. Chem. Soc*. **2019**, *141*, 15078–15091.

[22] J. M. Bollinger Jr, J. C. Price, L. M. Hoffart, E. W. Barr, C. Krebs, *Eur. J. Inorg. Chem*. **2005**, *2005*, 4245–4254.

[23] a) S. P. de Visser, *J. Am. Chem. Soc*. **2006**, *128*, 15809–15818; b) A. Decker, J.-U. Rohde, E. J. Klinker, S. D. Wong, L. Que Jr, E. I. Solomon, *J. Am. Chem. Soc*. **2007**, *129*, 15983–15996; c) S. Yeh, F. Neese, *Proc. Natl. Acad. Sci. USA* **2011**, *108*, 1228–1233.

[24] a) S. Shaik, S. Cohen, S. P. de Visser, P. K. Sharma, D. Kumar, S. Kozuch, F. Ogliaro, D. Danovich, *Eur. J. Inorg. Chem*. **2004**, *2004*, 207–226; b) D. C. Cummins, J. G. Alvarado, J. P. T. Zaragoza, M. Q. E. Mubarak, Y.-T. Lin, S. P. de Visser, D. P. Goldberg, *Inorg. Chem*. **2020**, *59*, 16053–16064.

[25] a) S. P. de Visser, S. Shaik, *J. Am. Chem. Soc*. **2003**, *125*, 7413–7424; b) D. Kumar, G. N. Sastry, S. P. de Visser, *J. Phys. Chem. B* **2012**, *116*, 718–730; c) S. Louka, S. M. Barry, D. J. Heyes, M. Q. E. Mubarak, H. S. Ali, L. M. Alkhalaf, A. W. Munro, N. S. Scrutton, G. L. Challis, S. P. de Visser, *J. Am. Chem. Soc*. **2020**, *142*, 15764–15779.

[26] E. F. Pettersen, T. D. Goddard, C. C. Huang, G. S. Couch, D. M. Greenblatt, E. C. Meng, T. E. Ferrin, *J. Comput. Chem*. **2004**, *25*, 1605−1612.

[27] *Gaussian*-09, Revision D.01, M. J. Frisch, G. W. Trucks, H. B. Schlegel, G. E. Scuseria, M. A. Robb, J. R. Cheeseman, G. Scalmani, V. Barone, B. Mennucci, G. A. Petersson, H. Nakatsuji, M. Caricato, X. Li, H. P. Hratchian, A. F. Izmaylov, J. Bloino, G. Zheng, J. L. Sonnenberg, M. Hada, M. Ehara, K. Toyota, R. Fukuda, J. Hasegawa, M. Ishida, T. Nakajima, Y. Honda, O. Kitao, H. Nakai, T. Vreven, J. A. Montgomery, Jr., J. E. Peralta, F. Ogliaro, M. Bearpark, J. J. Heyd, E. Brothers, K. N. Kudin, V. N. Staroverov, T. Keith, R. Kobayashi, J. Normand, K. Raghavachari, A. Rendell, J. C. Burant, S. S. Iyengar, J. Tomasi, M. Cossi, N. Rega, J. M. Millam, M. Klene, J. E. Knox, J. B. Cross, V. Bakken, C. Adamo, J. Jaramillo, R. Gomperts, R. E. Stratmann, O. Yazyev, A. J. Austin, R. Cammi, C. Pomelli, J. W. Ochterski, R. L. Martin, K. Morokuma, V. G. Zakrzewski, G. A. Voth, P. Salvador, J. J. Dannenberg, S. Dapprich, A. D. Daniels, O. Farkas, J. B. Foresman, J. V. Ortiz, J. Cioslowski, D. J. Fox, Gaussian, Inc., Wallingford CT, 2010.

[28] a) S. Ghafoor, A. Mansha, S. P. de Visser, *J. Am. Chem. Soc*. **2019**, *141*, 20278–20292; b) Y.-T. Lin, A. Stańczak, Y. Manchev, G. D. Straganz, S. P. de Visser, *Chem. Eur. J*. **2020**, *26*, 2233–2242; c) Y.-T. Lin, H. S. Ali, S. P. de Visser, *Chem. Eur. J*. **2021**, *27*, 8851–8864.

[29] a) A. D. Becke, *J. Chem. Phys*. **1993**, *98*, 5648–5652; b) C. Lee, W. Yang, R. G. Parr, *Phys. Rev. B* **1988**, *37*, 785–789.

[30] a) P. J. Hay, W. R. Wadt, *J. Chem. Phys*. **1985**, *82*, 270–283; b) W. J. Hehre, R. Ditchfield, J. A. Pople, *J. Chem. Phys*. **1972**, *56*, 2257–2261.

[31] M. Cossi, G. Scalmani, N. Rega, V. Barone, *J. Chem. Phys*. **2002**, *117*, 43–54.

[32] a) J. P. Perdew, M. Ernzerhof. K. Burke, *J. Chem. Phys*. **1996**, *105*, 9982–9985; b) A. Carlo, V. Barone, J. *Chem. Phys*. **1999**, *110*, 6158–6170.

[33] S. Grimme, J. Antony, S. Ehrlich, H. Krieg, *J. Chem. Phys*. **2010**, *132*, 154104.

Entry for the Table of Contents

Text for Table of Contents: Density functional theory calculations show how plant enzymes can initiate the biodegradation of herbicide molecules efficiently. However, the reactivity of substituted substrate analogues is slowed down and in some cases encounters a large rebound barrier.

Institute and/or researcher Twitter usernames: The University of Manchester (@OfficialUoM); Department of Chemical Engineering and Analytical Science (@UoMSciEng); Manchester Institute of Biotechnology (@UoMMIB)